Single Photon Avalanche Photodiodes for Near-Infrared Photon Counting

Mark A. Itzler, Xudong Jiang, Rafael Ben-Michael, Bruce Nyman, Krystyna Slomkowski
Princeton Lightwave Inc., 2555 US Route 130 South, Cranbury, NJ 08512

ABSTRACT

InP-based single photon avalanche diodes (SPADs) have proven to be the most practical solution currently available for many applications requiring high-performance photon counting at near-infrared wavelengths between 1.0 and 1.6 μm. We describe recent progress in the design, characterization, and modeling of InP-based SPADs, particularly with respect to the dark count rate vs. photon detection efficiency metric of devices optimized for use at both 1.55 μm and 1.06 μm. In this context, we report for the first time dark count probabilities as low as 7 x 10^{-7} ns^{-1} for fiber-coupled 1.55 μm SPADs operated at 20% detection efficiency and 215 K. Additionally, because of the critical role played by afterpulsing in limiting photon counting rates, we describe recent characterization of the dependence of afterpulsing effects on SPAD operating conditions such as photon detection efficiency, repetition rate, and bias gate length.

Keywords: avalanche photodiodes, single photon detector, SPAD, InP, InGaAs, 1.5 micron, 1.06 micron

1. INTRODUCTION

Strong interest in single photon detection at telecom wavelengths (e.g., 1.55 μm) is currently being driven by applications such as quantum information processing and quantum cryptography [1], and photon counting over the 1.0 to 1.6 μm wavelength range is highly desirable for lidar/ladar systems designed for remote sensing and ranging [2] as well as for free-space optical transmission in photon-starved applications [3]. For many applications such as these, InP-based single photon avalanche diodes (SPADs) have proven to be the most practical solution currently available for high-performance photon counting at near-infrared wavelengths between 1.0 and 1.6 μm. The devices exploit the behavior of an avalanche photodetector biased above its breakdown voltage, for which the creation of a single electrical carrier can induce a run-away avalanche that gives rise to a detectable macroscopic current. In this mode of operation, referred to as Geiger mode, the detector is sensitive to the absorption of a single photon. While there has been progress in the past few years in the area of InP-based SPADs for both 1.55 μm [4 – 9] and 1.06 μm [10 – 13] wavelengths, there is not yet a comprehensive understanding of underlying limitations to current InP/InGaAsP SPAD performance, and more comprehensive device experimentation and modeling is needed to guide optimization efforts.

In this paper, we describe recent progress in the design, characterization, and modeling of InP-based SPADs, particularly with respect to understanding and improving the dark count rate vs. photon detection efficiency metric of devices optimized for use at either 1.55 μm or at 1.06 μm. Good agreement between experimental and modeled results for the two SPAD structures optimized for detection at these two different operating wavelengths illustrates the utility of these modeling efforts. We report for the first time dark count probabilities as low as 7.5 x 10^{-7} ns^{-1} for fiber-coupled 1.55 μm SPADs operated at 20% detection efficiency and 215 K. Through modeling of the dependence of dark count rate on photon detection efficiency, we can identify the relative contribution of various dark carrier generation mechanisms in different layers of the SPAD structure as a function of operating temperature and voltage overbias. Additionally, because of the critical role played by afterpulsing in limiting practical photon counting rates, we show recent experimental characterization of the dependence of afterpulsing effects on a number of SPAD operating conditions, including photon detection efficiency, repetition rate, and bias gate length, with accompanying simulations that provide a useful description of afterpulsing effects.

2. SPAD DESIGN

Traditional optical receivers make use of linear mode avalanche photodiodes (APDs), for which the output photocurrent is linearly proportional to the intensity of the optical input. Applying a larger reverse voltage to the

Quantum Sensing and Nanophotonic Devices V, edited by Rengarajan Sudharsanan, Christopher Jelen,
Proc. of SPIE Vol. 6900, 69001E, (2008) · 0277-786X/08/$18 · doi: 10.1117/12.768564

avalanche detector will result in a larger gain, until the breakdown voltage V_{br} is reached. For bias voltages larger than V_{br}, the electron-hole generation process can become self-sustaining and result in an avalanche of charge limited only by external circuit resistance. In contrast to linear mode operation below V_{br}, if an avalanche photodetector is biased above V_{br}, then a single photoexcited carrier can induce a run-away avalanche that gives rise to an easily detectable macroscopic current. In this case, the detector is sensitive to a single photon input and is referred to as a single photon avalanche diode (SPAD). This mode of operation is often referred to as "Geiger mode" because of its similarity to Geiger-Muller detectors, in which particle emission from radioactive materials gives rise to an avalanche of carriers from ionized gas atoms.

Linear mode APD performance has a noise floor determined by the shot noise associated with leakage current, or dark current, that exists in the absence of input photons. Analogously, SPAD performance is degraded by false counts, or dark counts, that arise when carriers are created by processes other than photoexcitation. Both thermal excitation and field-mediated creation of free carriers (i.e., tunneling processes) contribute to the dark count rate (DCR). To improve the performance of SPADs in the presence of significant DCR, they are often operated in gated mode. The detector is biased at a baseline voltage just below the breakdown voltage, and to 'arm' the detector, a gate pulse is applied to bring the detector bias above breakdown for a short period of time, generally between 1 and 100 ns. For applications in which the photon arrival time is sufficiently well-known, a shorter gate pulse can be used to reduce the likelihood of a dark count being generated within the gate. However, for applications in which photon arrival times are not deterministic, the preferred operating mode is non-gated, or free-running, in which the detector is armed continuously until an avalanche event occurs.

Once an avalanche is initiated, it must be quenched. Gated quenching allows the avalanche to persist until the bias is reduced below V_{br} according to the fixed gate duration. For non-gated quenching, there are two primary techniques. Passive quenching employs a resistor in series with the APD so that the avalanche current induces a voltage across the resistor and drops the APD bias below V_{br}. Although this drop can be rapid, passive quenching often entails a rather long "reset" time dictated by the product of the quench resistance R and the detector capacitance C. Active quenching uses circuitry to force the APD bias below V_{br} once an avalanche is detected and then to actively reset the detector to its armed state in a time much shorter than the reset time corresponding to the passive quench RC time constant.

2.1 InP-based SPAD device structure

All InP-based avalanche photodetectors deployed today are based on the separate absorption and multiplication (SAM) regions structure [14]. We have developed a device design platform using the structure illustrated in Fig. 1 to fabricate SPADs optimized for single photon detection at 1.55 μm or at 1.06 μm. For 1.55 μm SPADs, we employ an $In_{0.53}Ga_{0.47}As$ ternary absorption layer with a 295 K cutoff wavelength of ~1.67 μm, while at 1.06 μm, we use an absorber consisting of a larger bandgap quaternary InGaAsP layer with a 295 K cutoff wavelength of ~1.2 μm. An n^+-InP buffer layer is grown on an n^+-InP substrate, followed by one of the two absorption layers just described. The valence band offset at an abrupt InGaAs(P)/InP heterojunction causes hole trapping [15], and InGaAsP grading layers are inserted between the absorber and the adjacent InP layer to reduce the effective trap depth for holes. Adjacent to the grading layers is a moderately doped field control layer that allows for flexible tailoring of the internal electric field profile in the device structure. The final epitaxial layer is an undoped InP cap layer. The active region is determined by patterning a SiN dielectric passivation layer to create a diffusion mask, and a subsequent diffusion of Zinc dopant atoms creates a p^+-InP region within the undoped InP cap layer. The thickness of the multiplication region is controlled by the Zn diffusion depth. A double diffusion process [16] is used to tailor the junction profile to avoid edge breakdown in the device periphery. With this buried junction design, the formation of a high-quality SiN passivation layer can guarantee low perimeter leakage and extremely stable long-life performance. The use of this platform for the fabrication of linear mode APDs is described further in [17] and references therein.

A primary goal of the design is to maintain low electric field in the narrower bandgap absorber (to avoid dark carriers due to tunneling) while maintaining sufficiently high electric field in the larger bandgap multiplication region (so that impact ionization leads to significant avalanche multiplication). The total integrated charge contained in the field control layer between the absorption and multiplication regions (the SACM structure [18]) is a critical design

parameter and must be optimized to achieve the desired electric field intensity at the SPAD's target operating temperature.

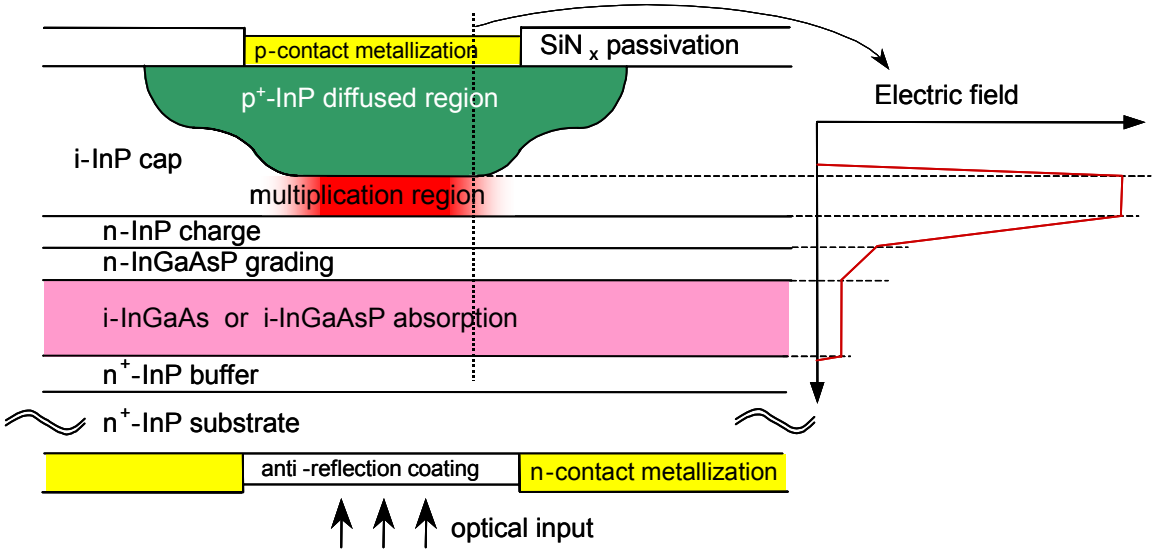

Figure 1. Schematic representation of SPAD design platform for single photon detection at either 1.55 µm or 1.06 µm.

2.2 Fiber-coupled SPAD modules

To achieve highly stable and robust fiber coupling to small (e.g., 25 µm) diameter SPADs, we have leveraged our existing capability for direct fiber coupling, with sub-micron tolerance, developed for the manufacturing of single mode diode lasers. The assembly technology that we have implemented allows us to guarantee high-yield, high-performance coupling using a fiber supported by a ferrule, with the ferrule held by a weld clip that is laser-welded with sub-micron positioning accuracy during an active alignment of the fiber to the detector. In Figure 2(a), we illustrate the hermetic 14-lead "butterfly"-style package with fiber feedthrough used as the SPAD module platform. In Figure 2(b), we show a micrograph identifying the main sub-components in the assembly. The SPAD is mounted to the side of an appropriate submount so that the ferruled fiber can be positioned orthogonal to the surface of the SPAD. Wrap-around leads on the submount provide convenient wirebond pads. The fiber is actively aligned using "grippers" controlled by a three-axis micropositioning system and is then fixed in place by laser welding the "weld clip" attached to the ferrule. The fiber is anchored in the ferrule using a solder glass attachment method. The presence of a thermistor directly adjacent to the SPAD-on-submount provides very accurate measurement of the SPAD temperature. This platform includes a single stage thermoelectric cooler (TEC) to augment the cooling provided by external TECs when using this device. Thermal cycling tests have shown that this module platform is highly reliable for operating temperatures at least as low as 200 K (–73 °C).

3. SPAD BEHAVIOR BELOW BREAKDOWN

The considerable differences between linear-mode and Geiger-mode operation dictate very distinct design requirements for SPADs relative to the more conventional InP-based linear-mode APDs [4]. Nevertheless, it is still of interest to consider whether certain aspects of linear mode behavior are indicative of good SPAD performance. In Figure 3, we illustrate the linear mode current-voltage (I-V) characteristics of a typical 25 µm active area diameter SPAD, where the active area diameter is determined by the more deeply diffused region that defines the multiplication region (see Figure 1). We operationally define the breakdown voltage V_{br} as the voltage for which the linear mode dark current I_d reaches 10 µA. The onset of the photocurrent response occurs when the p-n junction depletion first extends

into the InGaAs absorption region. The smooth increase in photocurrent, to gains in excess of 100 before V_{br} is reached, is consistent with a uniform gain profile and the absence of edge breakdown effects.

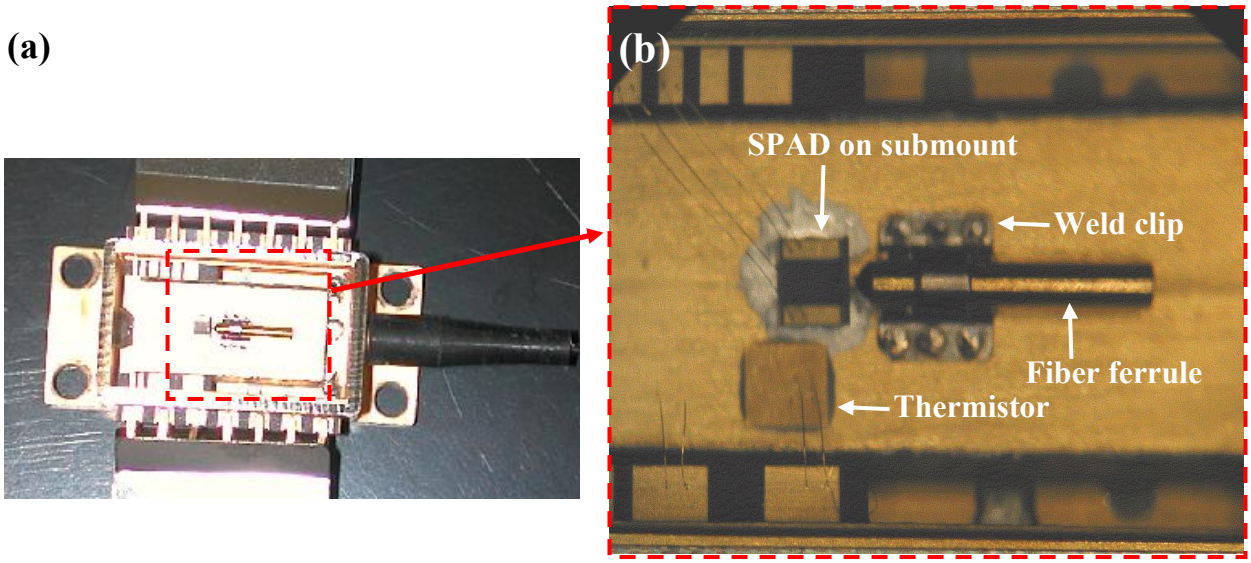

Figure 2. Photographs of (a) "butterfly"-style direct fiber coupled package enabling sub-micron accuracy of fiber positioning, and (b) blow-up of fiber coupling platform elements.

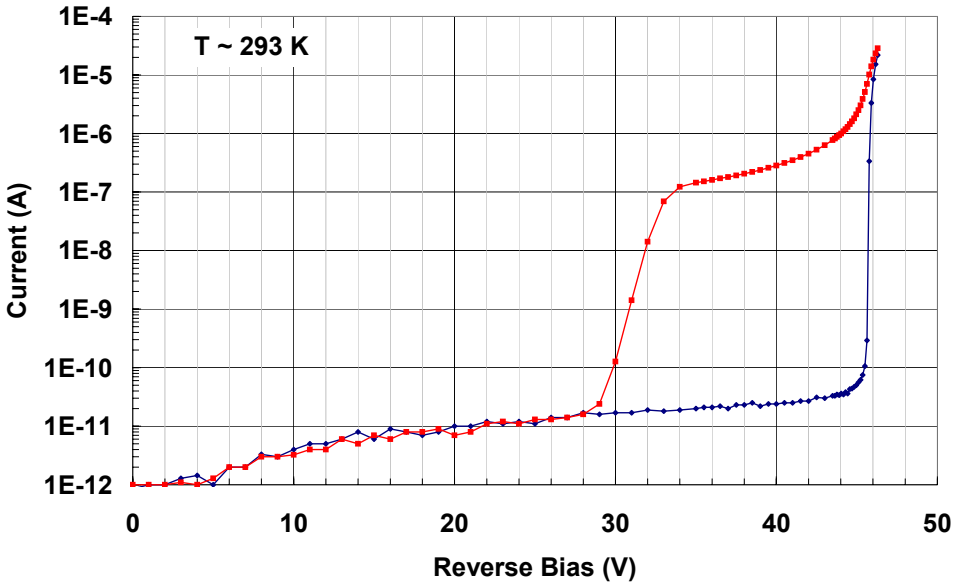

Figure 3. Room-temperature linear mode dark current and photocurrent I-V characteristics for a typical 1.55 μm SPAD. The photocurrent characteristic (upper curve) was obtained using ~100 nW of optical input power. Varying design criteria can dictate room-temperature breakdown voltages ranging from ~45 V (as in this figure) to as much as ~90 V (see Figure 4).

The dark I-V characteristic exhibits a number of significant features. Most importantly, I_d between ~20 V and a few volts below V_{br} is nearly independent of voltage. If I_d were dominated by bulk leakage from the narrow bandgap InGaAs or other layers (or interfaces) within the structure, this leakage current would be multiplied. In this case, we

would expect the shape of I_d to closely match the shape of the photocurrent I-V, which is determined almost exclusively by the multiplication of photo-excited carriers from the InGaAs. The absence of any apparent dark current multiplication until just before breakdown suggests that perimeter leakage currents dominate the dark current behavior in linear mode. We have confirmed for devices ranging from 25 μm to 1 mm taken from the same wafer that for sufficiently large diameters (i.e., 1 mm), bulk leakage dominates and dark I-V curves exhibit the same gain characteristic as photocurrent I-V curves. A very similar dominance of perimeter leakage in SPAD linear mode I-V characteristics has also been discussed in [8].

The DCR of a SPAD depends solely on bulk leakage since a dark carrier must pass through the multiplication region if it is to seed a run-away avalanche that will be detected as a dark count. I_d may be large due to significant perimeter leakage current (e.g., due to SiN passivation properties), but since only bulk leakage affects the DCR, the device may still exhibit good DCR. Alternatively, if I_d exhibits the same gain behavior as the photocurrent, then it is dominated by bulk leakage that will manifest itself in the DCR in Geiger mode. For a dark I-V characteristic which remains voltage-independent, its value just below breakdown provides only a worst case bound on SPAD DCR performance. Since bulk leakage contributes only a small fraction to the total dark current just below V_{br} in this case, the DCR will be much lower than would be calculated for an estimate of dark carrier generation based on the linear mode I_d.

To illustrate the spatial uniformity of our current SPAD fabrication process, we show the full-wafer mapping of breakdown voltage V_{br} for a recent 50-mm diameter 1.06 μm SPAD wafer in Figure 4. Device active area diameters vary from 40 μm to 200 μm, and the center-to-center die spacing is 400 μm.

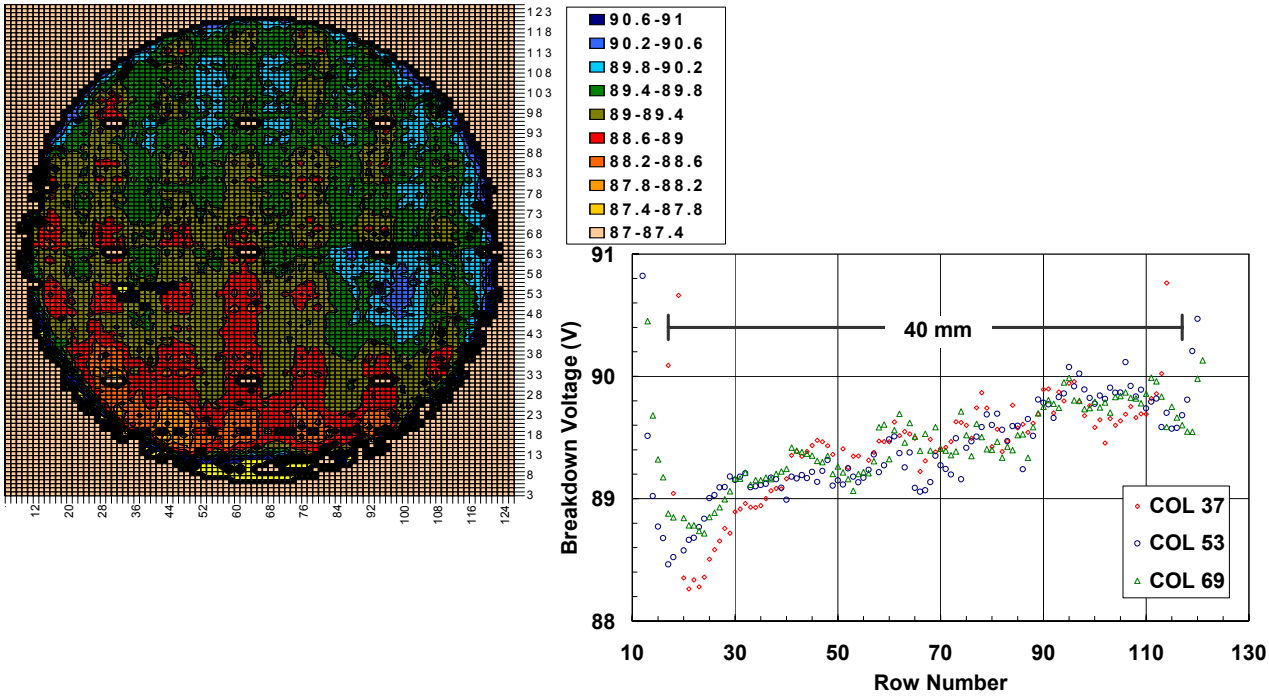

Figure 4. Full-wafer map of breakdown voltage for a 1.06 μm 50-mm diameter wafer. Average variation across the inner 40 mm of the wafer is ~1 V. Systematic variations based on an 8 x 8 die matrix were intentionally introduced to confirm a p-n junction diffusion control process. The graph shows data obtained from three columns of the wafer.

The overall variation in V_{br} across the inner 40 mm diameter of the wafer in the vertical direction (i.e., along die columns) is approximately 1 V. The variation along the horizontal direction (i.e., along die rows) is even smaller. The full-wafer map shows a short-scale systematic variation in V_{br} between neighboring areas consisting of 8 x 8 blocks of discrete die. These variations were intentionally introduced to confirm the effectiveness of a PLI patent-pending

approach to achieving highly precise dopant diffusion depth for controlling the vertical placement of the p-n junction in the SPAD structure. Figure 4 also contains a graph exhibiting more detailed data for V_{br} mapping along the direction of larger variation (i.e., vertically) by plotting individual V_{br} data points for devices along three columns of an identical device design, with 16 x 0.4 mm = 6.4 mm separation between successive columns. There is some minor short-scale fluctuation in V_{br}—some associated with the intentional design variations for diffusion control confirmation, and the rest most likely due to measurement error—but the average variation in V_{br} is ~0.031 V per mm. This level of device uniformity is highly desirable in utilizing this SPAD platform for the fabrication of single photon imaging arrays.

4. DARK COUNT PROBABILITY VS. PHOTON DETECTION EFFICIENCY

We directly measure DCR vs. PDE using a gated-mode measurement technique with short 1-ns gates at a repetition rate of 500 kHz. With this set-up, we employ a scheme in which "lit" and "dark" gates are interleaved so that DCR, PDE, and afterpulsing can be measured [19,20]. When this setup is operated with the source laser turned off, all the observed counts are dark counts. To obtain PDE and afterpulsing data, a pulsed diode laser source is synchronized so that single photons are temporally coincident only with the "lit" gate pulses; for clarity, we define all odd gates as "lit" gates and all even gates as "dark" gates. A laser source of the appropriate wavelength (i.e., 1.55 μm or 1.06 μm) is attenuated to generate a mean photon number of $\mu = 0.1$ per "lit" gate pulse, with a pulse full width at half maximum of 500 ps.

The DCR is obtained by measuring the dark count probability per gate in the absence of input photons. The PDE is determined by monitoring the total number of counts occurring in the odd "lit" gates when the single photon source is activated. During these lit measurements, an increase in the count rate found for the even "dark" gates (which are interleaved between the "lit" gates) above the intrinsic DCR indicates the presence of afterpulsing and can be used to quantify the afterpulse probability per gate.

4.1 Dark count rate vs. photon detection efficiency for 1.55 μm SPADs

The experimental data in Figure 5, indicated by symbols, were obtained using the short-gate (1-ns) measurement technique just described for four different 25 μm diameter InGaAs/InP SPADs at 1.55 μm using a 213 K operating temperature. These devices exhibit DCR values of about 10 kHz at a PDE of 20% at an overbias between 3 V and 4 V. (For reference, a DCR of 10 kHz is equivalent to a dark count probability per 1 ns gate of 1×10^{-5} ns^{-1}.)

To obtain a better understanding of the DCR vs. PDE behavior of our SPADs, we have performed theoretical modeling of the Geiger mode performance of these devices. Following the formalism of Donnelly, *et al.* [12], avalanche probabilities are calculated using field-dependent ionization coefficients. Non-local effects are neglected, as is valid for multiplication layer thicknesses ~1 μm and larger. Dark carrier generation is considered for all layers in the structure and includes temperature-dependent models for generation-recombination, band-to-band tunneling, and trap-assisted tunneling mechanisms. We calculate both the DCR and the PDE as a function of voltage overbias ΔV above the breakdown voltage V_{br}, and by using DCR and PDE values from successive ΔV, we can create simulated curves for DCR vs. PDE. Further details of our modeling approach can be found in [6]. As can be seen in Figure 5, the output of this modeling (solid line) provides good agreement with the experimental data obtained for DCR vs. PDE. At this operating temperature, thermal generation in the absorption layer and trap-assisted tunneling in the multiplication region both have a significant contribution to the total DCR. We will further illustrate the usefulness of the modeling results for identifying individual DCR mechanisms in our discussion of simulations for the 1.06 μm SPADs in the following sub-section.

Having the benefit of previous experimental work and supporting simulations, we have made significant recent improvements in the DCR vs PDE performance of 1.55 μm SPADs. In Figure 6, we summarize the performance of a typical distribution of fiber-coupled SPAD modules manufactured during the past several months. In the figure, we have indicated both dark count probability (DCP) per ns (left-hand axis) and DCR per second (right-hand axis) plotted as a function of PDE. A DCP performance of 1×10^{-5} ns^{-1} at 20% PDE was among the best devices seen for earlier

iterations of 1.55 µm SPADs (cf. Figure 5 above), and this most recent set of devices shows improvement of more than an order of magnitude for the highest performance devices.

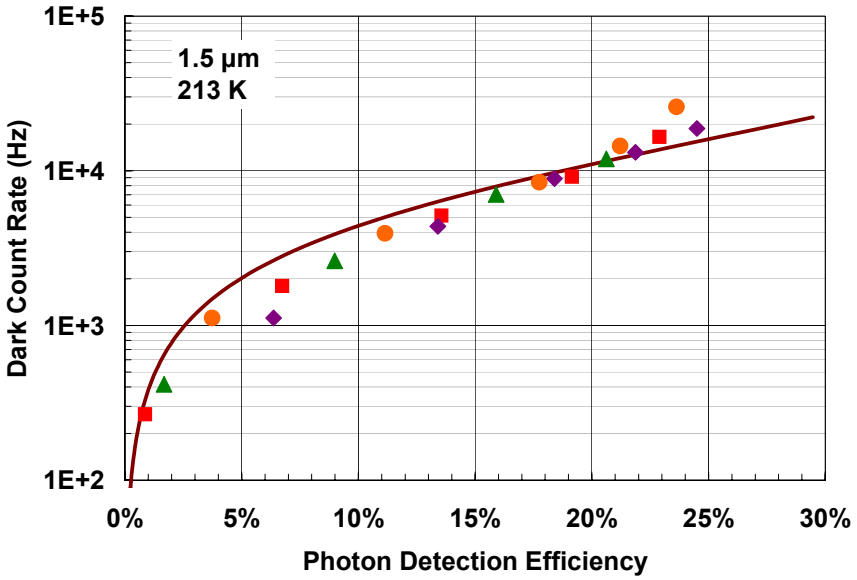

Figure 5. Dark count rate vs. photon detection efficiency for a 25 µm diameter InGaAs/InP SPAD at 1.55 µm and 213 K. Good agreement is seen between experimental data (symbols) from four different devices and modeling results (solid line).

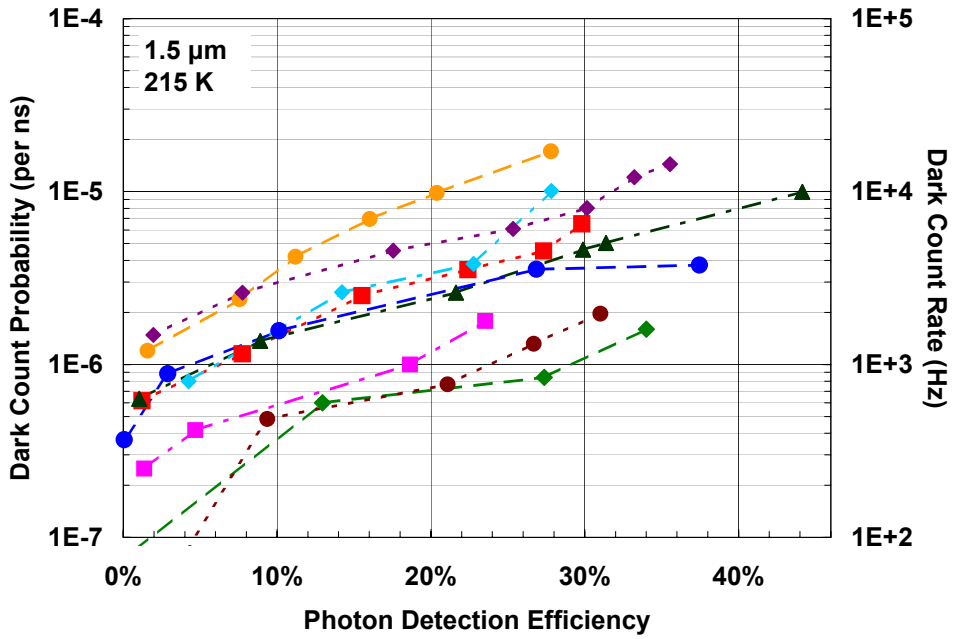

Figure 6. Dark count rate vs. photon detection efficiency for recent production run of 25 µm diameter SPAD fiber-coupled modules at 1.55 µm and 215 K. The highest performance of these devices represent the best dark count probability (7×10^{-7} ns^{-1} at 20% PDE) reported to date for a 1.55 µm SPAD.

The two best devices in Figure 6 exhibit a DCP of 7 x 10^{-7} ns^{-1}, corresponding to a DCR of 700 Hz, at a PDE of 20% for 215 K operation. We believe this is the best 1.55 μm SPAD performance reported to date for comparable operating conditions. The maximum PDEs shown are limited only by the 3 V to 4 V overbias limitation of our drive circuitry. Within this overbias range, a majority of the devices reach at least 30% PDE, where the best performance seen for DCP is ~ 1 x 10^{-6} ns^{-1}.

4.2 Dark count rate vs. photon detection efficiency for 1.06 μm SPADs

Using the device platform illustrated schematically in Figure 1, we have also designed and fabricated InGaAsP/InP SPADs optimized for operation at 1.06 μm. The primary difference between these devices and the 1.55 μm SPADs is the use of a larger bandgap quaternary InGaAsP absorption layer in place of the ternary InGaAs absorber used in the 1.55 μm device. However, the resulting difference in the behavior of thermal dark carrier generation in the InGaAsP absorber requires a complete re-optimization of the SPAD structure. To this end, the modeling techniques mentioned above have been of great value.

In modeling DCR, thermal and tunneling mechanisms were quantitatively considered in all layers of the structure. Figure 7 illustrates the calculated dependence on overbias ΔV of the total DCR as well as the contribution to DCR per unit area of the four principal layers of the 1.06 μm SPAD structure, i.e., the multiplication, field control, grading, and absorption layers, at 230 K and 250 K. These layer-by-layer calculations show that, as for the 1.55 μm SPADs, the dominant contribution to DCR originates from either (i) trap-assisted tunneling (TAT) in the multiplication region or (ii) thermal generation in the absorption layer. The relative importance of multiplication region TAT and absorption region thermal generation depends on the operating temperature and overbias. As seen in Figure 7(a), at 230 K, multiplication region TAT and absorption region thermal generation contribute on an equal footing for moderate overbias voltages between 1 V and 4 V. In contrast, by 250 K, Figure 7(b) illustrates that for ΔV less than 4 V, absorption layer thermal generation is fairly dominant.

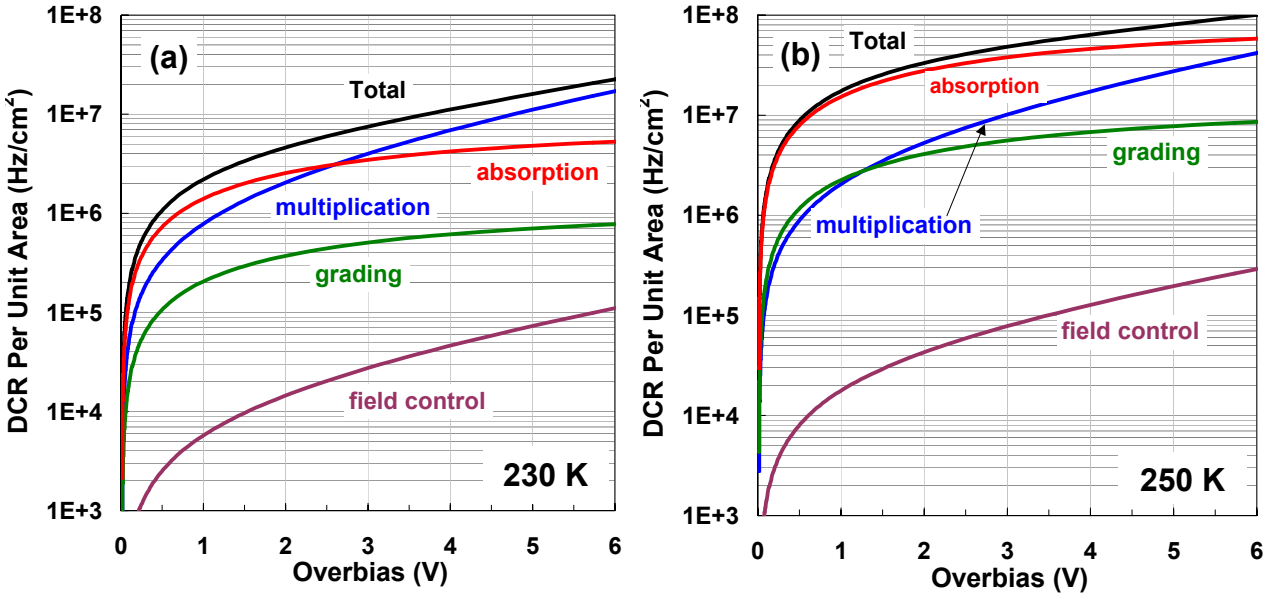

Figure 7. Calculated dependence of dark count rate (DCR) per cm^2 on overbias for 1.06 μm SPAD at (a) 230 K and (b) 250 K illustrated by curve labelled "total". Contribution to DCR of various layers is indicated, with dominant contributions seen from multiplication region trap-assisted tunneling and absorption region thermal generation. By 250 K, the DCR from the absorption layer in (b) is fairly dominant at overbias values below 4 V.

Our simulations for both the 1.55 μm and 1.06 μm SPADs have made use of the same materials parameters wherever equivalent materials exist in the structure. Three important parameters—SRH lifetime τ_{SRH}, trap density N_{trap}, and trap

energy level E_{trap}—must be determined by fitting of the model to experiment or by assuming values from the relevant literature. From fitting of our simulated results to the measured data, we find $\tau_{SRH} \sim 70$ µs, in reasonable agreement with literature values for InGaAs. The identification of trap densities and energy levels is important to the accuracy of this modeling, and although there have been past studies of the traps in InP and $In_{0.53}Ga_{0.47}As$, there is a wide variation in reports of the type, capture cross section, energy level, and concentration of traps in epitaxially grown samples of these materials. Therefore, following Donnelly *et al.* [12], we define a parameter $\alpha = (E_{trap} - E_{v0})/E_g$ to identify the position of traps inside the energy bandgap, where E_{trap} is the energy level of trap and E_{v0} is the top of valence band. We have found the simulation results to be particularly sensitive to the InP trap level $\alpha(InP)$, and to achieve fits for both SPAD structures (i.e., 1.55 µm and 1.06 µm), we have used a trap level value of $\alpha(InP) \sim 0.78$. This value is in reasonably good agreement with the value of $\alpha(InP) \sim 0.75$ reported in [7] and [12].

In Figure 8, we show DCR vs PDE at three temperatures for a 1.06 µm SPAD with a fairly large diameter of 80 µm. The figure also contains simulation results for DCR vs. PDE for the three experimental temperatures used. It is interesting to note that the performance of this 1.06 µm SPAD at 250 K is comparable to the very best of the 1.55 µm SPADs in Figure 6 even though the operating temperature is 35 K higher and the effective optical device area is at least substantially larger (i.e., 80 µm vs. 25 µm). This comparison emphasizes the extent to which SPAD performance can be improved if a wider bandgap absorbing material can be used in shorter cutoff wavelength applications.

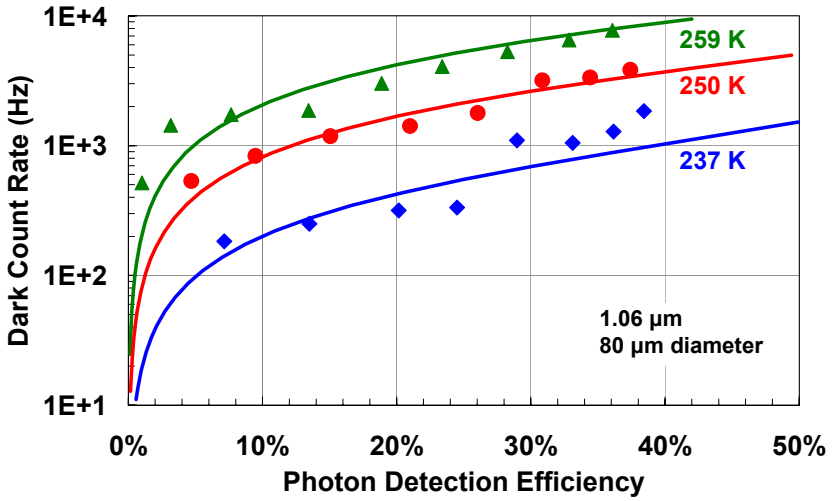

Figure 8. Dark count rate vs. photon detection efficiency for an 80 µm diameter InGaAsP/InP SPAD at 1.06 µm for three different temperatures. Experimental data at 259 K (triangles), 250 K (circles), and 237 K (diamonds) show good agreement with modeling results (solid lines).

5. CHARACTERIZATION OF AFTERPULSING EFFECTS

In a SPAD, the triggering of an avalanche event by a single photo-excited or dark-generated carrier results in the flow of a large number of impact-ionized carriers before the avalanche is quenched. The presence of defects in the multiplication region can lead to the trapping of at least a small fraction of these carriers. If the SPAD is quenched and re-armed before all of the trapped carriers have detrapped and drifted out of the multiplication region, it is possible for detrapped carriers to seed subsequent avalanches. Counts initiated by detrapped carriers are referred to as "afterpulses" and will increase the overall dark count rate. The most common technique for mitigating afterpulsing is the use of a "hold-off" time following the quenching of the SPAD during which the voltage bias is held below breakdown to prevent new avalanches from occuring while trapped carriers are detrapping. With a sufficiently long hold-off time, the probability of afterpulses occuring can be kept arbitrarily small. However, the use of longer hold-off times reduces the repetition rate at which counts can be obtained. If the "hold-off" time between gate quenching and re-arming is made too short, the measured DCR will increase sharply due to afterpulsing effects. The time scale for

this critical hold-off time is related to the characteristic de-trap time τ_d. To the extent that detrapping is thermally induced, τ_d can be reduced by operating at higher temperature, albeit at the expense of increased background DCR.

One of the most critical factors influencing afterpulsing is the total number of carriers that flow during an avalanche. The number of trapped carriers per avalanche is generally proportional to this total charge flow, and the probability of an afterpulse occuring will scale with the number of trapped charges [21]. Therefore, one of the principal strategies for reducing afterpulsing is to minimize the avalanche size. For instance, operation at lower overbias voltages generates smaller avalanches, and therefore less afterpulsing [4], but at the expense of reduced detection efficiency.

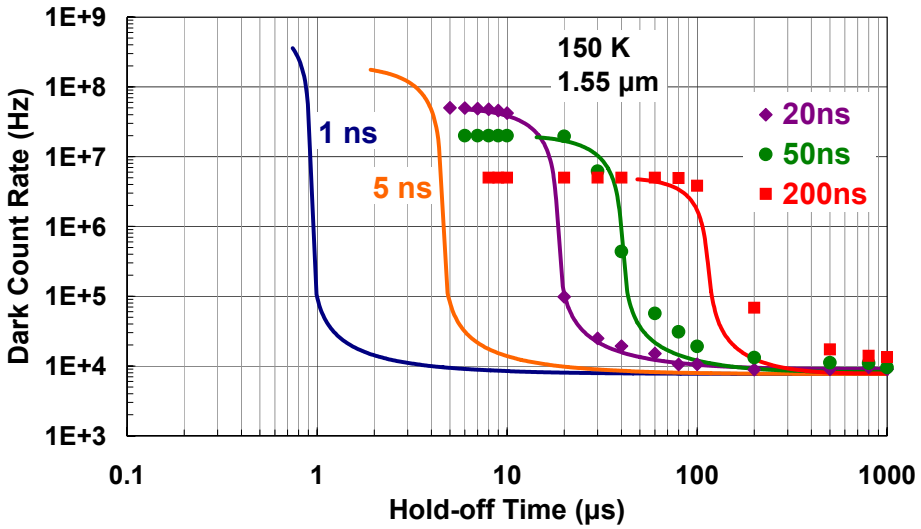

Figure 9. Dark count rate vs. hold-off time clearly illustrates impact of afterpulsing effects as a dramatic increase in DCR for sufficiently short hold-off times. Experimental [22] data (symbols) and simulated (solid lines) results are shown for a range of overbias gate lengths used in gated mode operation. The hold-off time at which the DCR increase occurs depends on the gate length used. The DCR saturates at a count rate for which there is at least one dark count during every bias gate.

Another operating condition that can have a significant effect on the number of carriers flowing per avalanche is the length of time in which an overbias gate is applied in gated mode operation. In Figure 9, we show experimental data and model results that illustrate the impact of gate duration on afterpulsing, which is evident as a dramatic increase in DCR for hold-off times shorter than a critical hold-off time determined by operating conditions. The experimental data [22], presented as symbols, show that for a gate length of 200 ns, the critical hold-off time for DCR increase is ~200 µs, whereas for much shorter gates of 20 ns, the critical hold-off time is ~ 20 µs. It is important to note that for these measurements, the gate was applied for the entire period indicated; that is, there was no active quenching during the gate immediately following the detection of an avalanche, as is often used to minimize current flow [23]. Since there is a uniform probability for an avalanche to occur (seeded by a dark carrier generation event) at any point during the gate duration, the average duration for current flow will be one-half of the gate duration (e.g., 100 µs of average current flow for the 200 µs gate). These measurements were carried out at a rather low temperature of 150 K, which results in stronger afterpulsing effects than would be found at more typical operating temperatures provided by thermoelectric coolers (e.g., 200 – 225 K) [4].

Also illustrated in Figure 9 are the results of simulations (solid lines) we have performed using a model developed by Kang *et al.* [24] to quantify the afterpulsing contribution to DCR for periodic gated mode operation. One finds the dark count probability $P_d = 1 - \exp(-N_d P_a)$ assuming Poisson statistics. P_a is the calculated probability that a carrier triggers a detectable avalanche, and the mean number of dark carriers N_d contains contributions from two types of dark carriers. Primary dark carriers are generated during a gate pulse and cause a dark count within that gate pulse. Afterpulse dark carriers are carriers generated and trapped during a previous gate pulse that are released during the

gate pulse under consideration. To obtain an accurate description of afterpulsing dark carrier generation, the model includes the contribution of trapped carriers from all previous gate pulses by summing over all of these previous gates.

As seen in Figure 9, this afterpulsing model gives us reasonable agreement with the experimental data shown, for gate widths of 20, 50, and 200 µs. The somewhat steeper rise in DCR with decreasing hold-off time seen in the simulation results may be due to the fact that we have included only a single de-trapping time for the model results presented here. We can achieve an even more accurate fit by assuming a second dominant de-trapping time, and from the literature on deep level traps in InP as well as recent afterpulsing studies [8], there may be justification for the assumption of multiple trap levels. However, in the context of the current work, the results of the single trap model provide adequate physical insight into the afterpulsing behavior exhibited in Figure 9. For instance, we expect to find that the DCR vs. hold-off time behavior for our short 1-ns gate measurements described at the beginning of Section 4 will exhibit a degradation in afterpulsing behavior only for hold-off times shorter than ~ 1 µs. Experimental results of 1-ns gate measurements are shown in Figure 10. From these data, it is seen that the afterpulse probability is still acceptable (e.g., 0.01 at 20% PDE) up to a 5 MHz repetition rate, which corresponds to a 0.2 µs hold-off time. However, a doubling of the repetition rate, to 10 MHz, causes the afterpulse probability to jump by more than an order of magnitude, indicating that an effective hold-off time between 0.1 and 0.2 µs is the critical value below which afterpulsing degrades sharply.

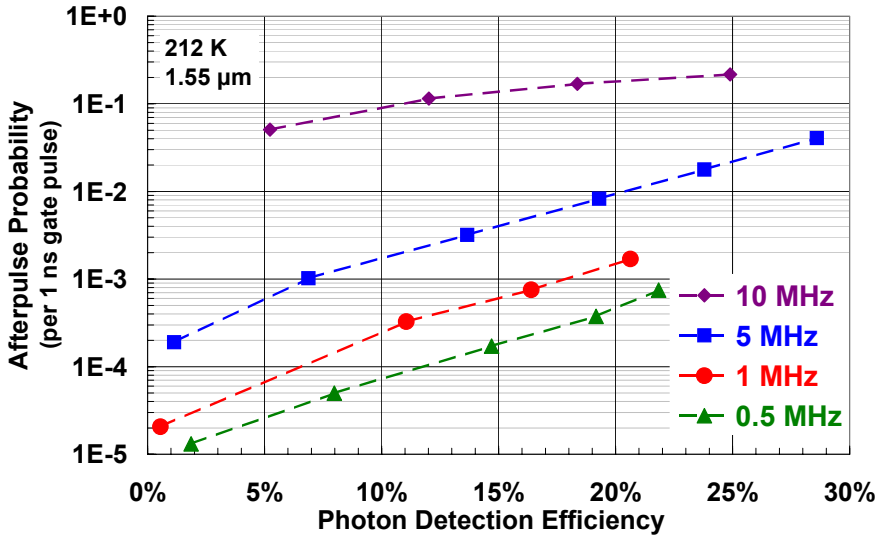

Figure 10. Afterpulsing probability per 1 ns gate pulse vs. photon detection efficiency for repetition rates of 0.5, 1, 5, and 10 MHz using the short-gate measurement technique describes at the beginning of Section 4.

6. CONCLUSIONS

In describing recent progress in the design, characterization, and modeling of InP-based SPADs, we have shown good agreement between experimental data and modeling results for the dark count rate vs. photon detection efficiency metric of devices optimized for use at 1.55 µm and at 1.06 µm. The modeling indicates that the two dominant dark count generation mechanisms are thermal generation in the narrow bandgap absorption layer and trap-assisted tunneling in the wider bandgap InP multiplication layer. The relative importance of these two mechanisms depends on both temperature and bias. For 1.55 µm SPADs, we have shown what we believe to be the lowest dark count probabilities reported to date, with values as low as 7.5 x 10^{-7} ns^{-1} for fiber-coupled modules at 20% detection efficiency and 215 K. At 1.06 µm, typical device performance improves by nearly two orders of magnitude relative to 1.5 µm SPADs through the use of a wider bandgap InGaAsP absorption region. These devices are quite promising for a variety of applications at 1.06 µm since they exhibit photon detection efficiency larger than that Si SPADs by a factor ~10 simultaneously with low DCR (assuming moderate thermoelectric cooling) comparable to that of Si SPADs. Finally, we have shown how SPAD afterpulsing in gated mode operation is highly dependent on gate width as well as

gate repetition rate. Modeling of the afterpulsing behavior gives a good description of the afterpulsing effects seen in the dependence of DCR on hold-off time. We also show that with short 1-ns gating, we can operate at gate frequencies of at least 5 MHz with acceptable afterpulsing probabilities (0.01 at 20% PDE). The dramatic increase in afterpulse probability between 5 MHz and 10 MHz gate frequencies is consistent with modeling results.

REFERENCES

[1] N. Gisin, G. Ribordy, W. Tittel, and H. Zbinden, "Quantum cryptography", *Rev. Mod. Phys.*, vol. 74, no.1, pp. 145-195 (2002).

[2] R. M. Measures, Laser Remote Sensing - Fundamentals and Applications, John Wiley & Sons (1984).

[3] Special Issue on "Free-space laser communications", IEEE LEOS Newsletter, vol. 19 No. 5 (2005).

[4] M. A. Itzler, R. Ben-Michael, C.-F. Hsu, K. Slomkowski, A. Tosi, S. Cova, F. Zappa, and R. Ispasoiu, "Single photon avalanche diodes (SPADs) for 1.5 μm photon counting applications*", J. Mod. Opt*., vol. 54, no. 2-3, pp. 283-304 (2007).

[5] X. Jiang, M. A. Itzler, R. Ben-Michael, K. Slomkowski, "InGaAsP avalanche photodetectors for near IR single photon detection," *Proceedings of the SPIE* **6771**, 677127 (2007).

[6] X. Jiang, M. A. Itzler, R. Ben-Michael, K. Slomkowski, "InGaAsP-InP Avalanche Photodiodes for Single Photon Detection," *IEEE Sel. Topics in Quantum Electron.* vol. 13, p. 895 – 905 (2007).

[7] S. Verghese, J. P. Donnelly, E. K. Duerr, *et al.*, "Arrays of InP-based Avalanche Photodiodes for Photon Counting," *IEEE Sel. Topics in Quantum Electron.* vol. 13, p. 870 – 886 (2007).

[8] M. Liu, C. Hu, X. Bai, X. Guo, J. C. Campbell, Z. Pan, and M. M. Tashima, "High-performance InGaAs/InP single-photon avalanche diode," *IEEE Sel. Topics in Quantum Electron.* vol. 13, p. 887 – 894 (2007).

[9] S. Pellegrini, R.E. Warburton, L.J.J. Tan, J.S. Ng, A.B. Krysa, K. Groom, J.P.R. David, S. Cova, M.J. Robertson, and G.S. Buller, "Design and performance of an InGaAs-InP single-photon avalanche diode detector", *IEEE J. Quantum Electron.*, vol. 42, no. 4, p. 397-403, Apr. 2006.

[10] X. Jiang, M. A. Itzler, R. Ben-Michael, K. Slomkowski, M. A. Krainak, S. Wu, and X. Sun, "Afterpulsing effects in free-running InGaAsP single photon avalanche diodes," *IEEE J. Quantum Electron*., vol. 44, pp. 3 – 11 (2008).

[11] M. A. Itzler, X. Jiang, R. Ben-Michael, K. Slomkowski, M. A. Krainak, S. Wu, and X. Sun, "InGaAsP avalanche photodetectors for non-gated 1.06 μm photon-counting receivers," *Proceedings of the SPIE* **6572**, 65720G (2007).

[12] J. P. Donnelly, E. K. Duerr, K. A. McIntosh, et al., "Design Considerations for 1.06-μm InGaAsP-InP Geiger-Mode Avalanche Photodiodes," IEEE J. Quantum Electron., vol. 42, 797-809 (2006).

[13] K.A. McIntosh, J. P. Donnelly, D.C. Oakley, et al., "InGaAsP/InP avalanche photodiodes for photon counting at 1.06 μm," Appl. Phys. Lett., vol. 81 2505-2507 (2002).

[14] K. Nishida, K. Taguchi, and Y. Matsumoto, "InGaAsP heterostructure avalanche photodiodes with high avalanche gain," *Appl. Phys. Lett.*, vol. 35, 251–252 (1979).

[15] S. R. Forrest, O. K. Kim, and R. G. Smith, "Optical response time of $In_{0.53}Ga_{0.47}As$ avalanche photodiodes," *Appl. Phys. Lett.*, vol. 41, 95–98 (1982).

[16] Y. Liu, S.R. Forrest, J. Hladky, M. J. Lange, G. H. Olsen, and D. E. Ackley, "A Planar InP/InGaAs avalanche photodiode with floating guard ring and double diffused junction", *J. Lightwave Tech.*, vol. 10, no. 2, pp. 182-193, Feb. 1992.

[17] M. A. Itzler, K. K. Loi, S. McCoy, N. Codd, and N. Komaba, "High-performance, manufacturable avalanche photodiodes for 10 Gb/s optical receivers, " *Proc. of 25th Optical Fiber Communication Conference (OFC 2000)*, vol. 4, 126 – 128 (2000).

[18] J. C. Campbell, A. G. Dentai, W. S. Holden, and B. L. Kasper, "High-performance avalanche photodiode with separate absorption, 'grading', and multiplication regions, " *Electron. Lett.*, vol. 19, 818 – 820 (1983).

[19] R. Ben-Michael, M.A. Itzler, B. Nyman, and M. Entwistle, "Afterpulsing in InGaAs/InP single photon avalanche photodetectors", *2006 Digest of the LEOS Summer Topical Meetings*, pp. 15-16 (2006).

[20] D.S. Bethune, W.P. Risk, G.W. Pabst, "A high-performance integrated single-photon detector for telecom wavelengths", *J. Mod. Opt.*, vol. 51, no. 9–10, pp. 1359–1368, June 2004.

[21] K.E. Jensen, P.I. Hopman, E.K. Duerr, E.A. Dauler, J.P. Donnelly, S.H. Groves, L.J. Mahoney, K. A. McIntosh, K.M. Molvar, A. Napoleone, D.C. Oakley, S. Verfhese, C.J. Vineis, and R.D. Younger, "Afterpulsing in Geiger-mode avalanche photodiodes for 1.06 μm wavelength", *Appl. Phys. Lett.*, vol. 88, no. 13, 133503, Mar. 2006.

[22] Data provided by A. Tosi, F. Zappa, and S. Cova, unpublished.

[23] S. Cova, M. Ghioni, A. Lacaita, C. Samori, and F. Zappa, "Avalanche photodiodes and quenching circuits for single-photon detection", *Appl. Opt.*, vol. 35, no. 12, pp. 1956-1976, Apr. 1996.

[24] Y. Kang, H. X. Lu, Y.-H. Lo, D. S. Bethune, and W. P. Risk, "Dark count probability and quantum efficiency of avalanche photodiodes for single-photon detection," *Appl. Phys. Lett.*, **83**, 2955 (2003).